Experimental investigation of turbulent coherent structures interacting with a porous airfoil

Tamaro, Simone; Zamponi, R.; Ragni, D.; Teruna, C.; Schram, Christophe

Important note
To cite this publication, please use the final published version (if applicable).
Please check the document version above.

RESEARCH ARTICLE

Experimental investigation of turbulent coherent structures interacting with a porous airfoil

Simone Tamaro[1] · Riccardo Zamponi[1] · Daniele Ragni[2] · Christopher Teruna[2] · Christophe Schram[1]

Abstract

The flow field on solid and porous airfoils subjected to turbulence shed by an upstream cylindrical rod and the corresponding far-field noise radiations are studied through particle image velocimetry (PIV) and microphone measurements, respectively. Three different Reynolds numbers based on the rod diameter are considered in a range between 2.7×10^4 and 5.4×10^4, and two porous airfoil models are tested to analyze the influence of the design elements of the permeable treatment. A standard proper orthogonal decomposition (POD) algorithm is employed to band filter the different length scales that characterize the turbulent flow, making it feasible to determine which turbulence scales are affected by porosity. The aeroacoustic results indicate that the porous treatment of the wing profile leads to a noise reduction at low frequencies and a noise regeneration at high frequencies due to surface roughness. The investigation on the flow field shows that the main effect of porosity is to mitigate the turbulent kinetic energy in the stagnation region, attenuating the distortion of turbulence interacting with the airfoil surface. The application of the POD algorithm indicates that this effect acts mainly on the largest scales of turbulence.

Keywords Aeroacoustics · Turbulence-interaction noise · Porous materials · POD

1 Introduction

Turbulent flows interacting with solid surfaces constitute an efficient source of broadband noise. For a wing profile exposed to a significantly disturbed flow, the dominant source of noise comes from the interaction of turbulence with the leading edge of the wing profile (Migliore and Oerlemans 2004; Moreau and Roger 2005). This is usually the case for turbofan engines, cooling systems for automotive applications, and high-lift devices on aircraft wings.

Turbulence-interaction noise is generated by the rapid deformation of turbulent structures impinging on the surface of a wing profile (Roger et al. 2013). As a result of the interaction, a fraction of the kinetic energy of the turbulence eddies is scattered into sound and this effect is amplified in correspondence with a singular point of the flow, such as the leading edge of an airfoil. In this framework, Amiet

(1975) proposed a semi-analytical model for the prediction of the far-field sound power-spectral density (PSD) of an airfoil immersed in a subsonic turbulent flow. The author identified the spanwise correlation length of turbulence, a mathematically derived aeroacoustic transfer function based on geometric parameters that models the airfoil response and radiation, and the two-dimensional spectrum of the upwash velocity fluctuations as the main parameters contributing to the total sound-pressure level in the far-field. Furthermore, numerous experimental investigations (Paterson and Amiet 1976; Olsen and Wagner 1982; Migliore and Oerlemans 2004; Moreau and Roger 2005; Devenport et al. 2010) were performed with the aim to characterize the dependence of turbulence-interaction noise on the geometrical parameters of the airfoil. In particular, a common finding of these studies was that the levels of the leading-edge noise emissions depend significantly on the airfoil thickness—showing that an increase of this value leads to a strong noise reduction— and only marginally on airfoil camber and angle of attack.

In an industrial framework, inflow turbulence is typically produced by installation elements upstream of the wing profile that cannot be removed, such as grids or pipes. A possible technique for the airfoil-turbulence interaction noise mitigation is to make the acoustic response of the airfoil

✉ Simone Tamaro
   simone.tamaro@vki.ac.be

[1] von Karman Institute for Fluid Dynamics, Waterloosesteenweg 72, 1640 Sint-Genesius-Rode, Belgium

[2] Delft University of Technology, Kluyverweg 1, 2629 HS Delft, The Netherlands

less sensitive to turbulence by using porous materials. The application of these materials has proven to successfully mitigate the noise radiation, but further studies are required to improve the understanding of the physical mechanisms involved in the reduction, with the ultimate goal of developing novel acoustic mitigation techniques.

The idea of applying porosity for noise attenuation comes from studies on the silent flight of owls by Kroeger et al. (1972), who described the feather structure at the trailing edge of the owl wings as *wing porosity* and classified this as one of the mechanisms responsible to silence their flight. Recently, the implementation of porous materials in the airfoil structure has been treated both numerically and experimentally with successful results in terms of noise mitigation (Geyer et al. 2011, 2012; Roger et al. 2013; Roger and Moreau 2016; Zamponi et al. 2019; Satcunanathan et al. 2019; Paruchuri et al. 2020; Teruna et al. 2020). The noise reduction performance was generally found to be highly dependent on the frequency range considered, with reductions in sound-pressure levels of up to 6 dB in the far-field at low frequencies. On the contrary, the application of porosity has not been found to be as effective at high frequencies, where the increase in surface roughness typically associated with porous surfaces leads to a noise regeneration if compared to impermeable wing profiles.

Furthermore, the implementation of porosity into the structure of an airfoil is responsible for a penalization of its aerodynamic performance in terms of lift and drag (Geyer et al. 2010). Specifically, the lift force decreases due to the flow penetration that allows for the communication between pressure and suction side of the wing profile, whereas the drag force increases due to the augmented surface roughness and the unsteady flow transportation through the permeable material. Studies on the quantification of the aerodynamic performance loss associated with porosity have been provided by Sarradj and Geyer (2007) and Teruna et al. (2020). Recently, technological solutions for the implementation of porous materials in the structure of the airfoil have been proposed with the aim of mitigating the degradation of aerodynamic performance. These technologies include permeable exoskeletons (Zamponi et al. 2019) and solid centerplanes (Roger and Moreau 2016; Bampanis and Roger 2020) to control surface roughness and flow penetration.

Although a clear agreement over the physical mechanisms that govern the noise reduction achieved with porous media has not been reached yet, some hypotheses have been formulated. A possible mechanism involves the hydrodynamic absorption by the porous medium that is responsible for a weakened distortion of inflow turbulence in proximity to the leading edge. This possibility has been investigated by Zamponi et al. (2020), who performed hot-wire anemometry measurements of the unsteady flow around a porous NACA-0024 profile to characterize the distortion of turbulence interacting with the airfoil. Results indicated a significant effect of porosity on the turbulent velocity within the stagnation region, with a pronounced reduction of velocity fluctuations in the upwash component. This effect was mostly confined to the low-frequency range of the turbulent velocity spectrum, with a trend similar to that of the far-field noise mitigations measured through acoustic beamforming. The authors suggested that the attenuated distortion experienced by turbulence in the proximity of the airfoil leading edge may be associated to less efficient conversion of vortical energy of the turbulent eddies into sound.

The aim of the present work is to further investigate the effect of porosity on the turbulence distortion by separating the different turbulence scales that constitute the flow. This objective is pursued through the use of an advanced post-processing technique based on the proper orthogonal decomposition (POD), which is a data compression tool first applied in the context of turbulence by Lumley (1967). Recently, the POD has been extensively employed to isolate and identify coherent structures within a turbulent flow. Jacob et al. (2005) applied this method to a rod–airfoil configuration and underlined the contribution of a limited number of modes that account for the majority of the total energy of the flow. Furthermore, the POD has been adopted in many studies to inspect the large scales of turbulence. Tandalam et al. (2010) used the most energetic POD modes to reconstruct a turbulent jet flow and showed that it is possible to filter out small coherent structures according to the considered number of modes. Similar findings have also been found by Deri et al. (2014), while Raiola et al. (2015) proposed an application of the POD to filter out the random error component of PIV. New variants of the POD algorithm have recently proposed to improve the detection of coherent structures and the separation of their respective scales by expressing the POD in the frequency domain (Towne et al. 2018) and by optimizing modes within a target frequency range (Mendez et al. 2020).

The experimental analysis presented in the paper includes far-field acoustic measurements for the evaluation of the noise reduction performance that can be achieved with the porous treatment of a NACA-0024 profile installed in a rod–airfoil configuration. The effect of the Reynolds number is also analyzed. In addition, time-resolved particle image velocimetry (PIV) measurements are performed to investigate the impact of porosity on the flow field. The turbulence statistics and the one-dimensional velocity spectra related to the different scales of the turbulent flow are finally compared by means of the POD algorithm.

The paper is structured as follows: Sect. 2 presents the experimental setup and the applied methodology. In Sect. 3, the main experimental results are shown and discussed. The conclusions of the investigation are drawn in Sect. 4.

2 Materials and methods

2.1 Design of the airfoils

The airfoil models considered in the experiments are symmetric NACA-0024 profiles, designed and manufactured at the von Karman Institute for Fluid Dynamics (VKI). They are characterized by a chord length of 0.157 m, a span of 0.200 m, and a maximum thickness of 0.038 m. The baseline airfoil (labeled as *solid airfoil*) presents an impermeable hard-plastic exoskeleton that ensures the shape integrity of the NACA-0024 profile. In the porous configuration (labeled as *porous airfoil*), the exoskeleton features hexagonal pores allowing for flow penetration into the airfoil inner volume, which is filled in with melamine foam. A sketch of this configuration is shown in Fig. 1. A solid centerplane is installed along the chord line, from the trailing edge up to 1 radius of curvature of distance from the leading edge $R_{LE} \approx 0.01$ m in order to avoid cross-flow between the suction and the pressure side of the airfoil.

In this way, the lift force of the wing profile, which results from the static pressure difference between pressure and suction sides, is less likely to be degraded by the porous treatment when a nonzero angle of attack is considered. The present effect has been investigated by Zamponi et al. (2020), who measured the static pressure distribution on the wing profile surface at 0° angle of attack. The results showed that the presence of porosity brings a slight reduction of the flow displacement by the airfoil that partially levels out the pressure differences along the surface. However, the C_p deviation between solid and porous models appears to be limited by the presence of the exoskeleton that effectively preserves the integrity of the NACA-0024 profile's shape.

Both airfoil configurations are coated with a metallic woven wire mesh to ensure the same surface roughness. Additional details about the design of these components can be found in Zamponi et al. (2020). Moreover, a third airfoil (labeled as *melamine airfoil*) has been designed to investigate the impact of the exoskeleton and the wire mesh on nois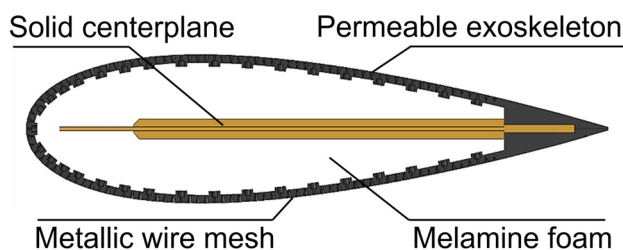e reduction. In this case, the melamine foam has been cut in the shape of a NACA-0024 profile and glued directly on the solid centerplane.

The parameters defining the porous medium play an important role in the noise reduction performance that can be achieved by means of porosity (Geyer et al. 2011). The characterization of the melamine foam employed in the design of the porous airfoils has been performed using an inverse method based on the measurement of the scattering matrix (Niskanen et al. 2017) and is discussed in details by Satcunathan et al. (2019). The main resulting parameters are listed in Table 1.

2.2 Experimental setup

2.2.1 Wind tunnel

The experimental work presented in this section is carried out at the A-tunnel facility of Delft University of Technology (TUD), an open-jet, closed-circuit, anechoic vertical wind tunnel. A rod–airfoil configuration is chosen for the presented measurement campaign. This is a typical experimental aeroacoustic arrangement first proposed by Jacob et al. (2005) as a benchmark test case, in which the generated acoustic spectrum is broadband and dominated by a distinctive shedding frequency.
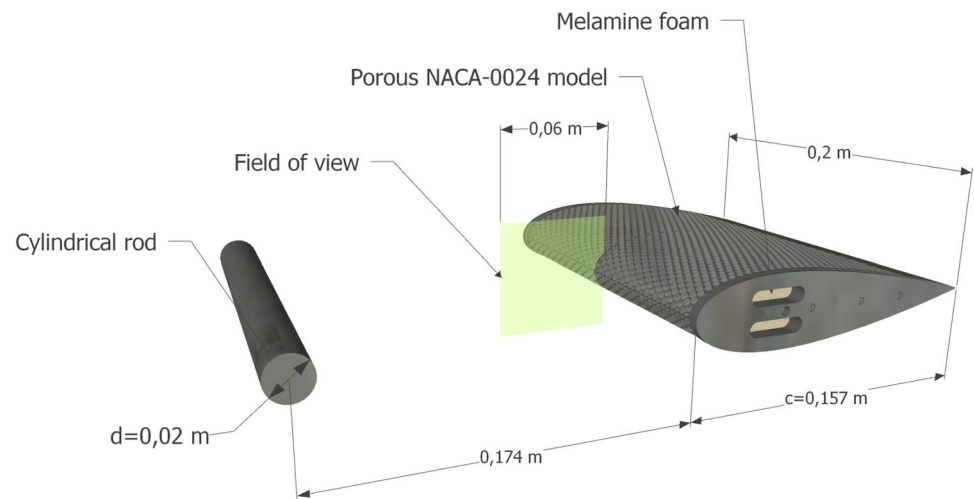
The airfoil models and the cylindrical rod are held in position by two side plates installed on a 3D-printed outlet nozzle with a rectangular exit plane of 0.25 m × 0.40 m. The nozzle flow is characterized by a turbulence intensity below 0.1% for free-stream velocities higher than 20 ms^{-1} in the absence of turbulence generation. Further information about the wind tunnel design and the nozzle flow characteristics can be found in Merino-Martinez et al. (2020), while a sketch of the rod–airfoil configuration is depicted in Fig. 2. The cylindrical rod has the same diameter as the airfoil leading-edge circle amounting to $d = 0.020$ m and is placed in the potential core of the jet 0.174 m upstream of the airfoil leading edge. A 3D-printed extension with the shape of the NACA-0024 profile and a length of 0.050 m is designed to adapt the 0.200 m span of the airfoils with the 0.250 m of the wind tunnel.

The experiments are carried out at 0° angle of attack and at free-stream velocities of $U_\infty = 20$ ms^{-1}, $U_\infty = 30$ ms^{-1}, and $U_\infty = 40$ ms^{-1} corresponding to rod-based Reynolds numbers of 2.7×10^4, 4.1×10^4, and 5.4×10^4, respectively.

Fig. 1 Section of the porous NACA-0024 airfoil model employed in the PIV experimental campaign. Adapted from Zamponi et al. (2020)

Table 1 Porous parameters characterizing to the melamine foam integrated in the porous airfoil models: static air flow resistivity σ, porosity ϕ, tortuosity α, and static permeability k_0 (Satcunathan et al. 2019)

σ Pa s m^{-2}	ϕ [−]	τ [−]	k_0 [m^2]
8.683×10^3	0.986	1.02	1.942×10^{-4}

2.2.2 Aeroacoustic measurements

Aeroacoustic measurements are performed using the data acquired by 64 G.R.A.S. *40PH* analog free-field microphones with a flat frequency response of ± 1 dB from 50 Hz to 5 kHz and of ± 2 dB up to 20 kHz, calibrated in amplitude and phase through a G.R.A.S. *42AA pistonphone* and a clapping device that generates an impulse broadband sound.

The microphones are installed on a steel perforated plate parallel to the span of the airfoil, at a distance of 1 m from its chord line. Further details on the microphone array employed in the campaign are provided in Merino-Martinez et al. (2020). Data have been acquired at 50 kHz, while the spectra have been computed with the *Welch method* (Welch 1967), using windows of 2^{13} data points and 50% overlap.

2.2.3 PIV measurements

Stereoscopic time-resolved PIV measurements are taken on a plane at the midspan of the airfoils, centered in the stagnation region. Two *Photron* Fastcam SA 1-1 with a pixel (px) pitch of 20 μm and a sensor of 1024×1024 px^2 are used with an exposure time of 185 μs. The cameras are equipped with Nikon *NIKKOR* 105 mm focal distance macro-objectives set at an f-number of $f_\# = 5.6$. Seeding is produced by a SAFEX *Twin-Fog Double Power* fog generator with a glycol-based solution. The generated mean drop diameter is 1 μm.

The laser sheet is obtained through laser pulses with a wavelength of 527 nm and energy of 30 μJ per pulse that are generated by a Quantronix *Darwin Duo 527-80-M double cavity Nd:YLF system* using a spherical and a cylindrical optical lens, resulting in an approximate thickness of 1 mm. The field of view (FOV), visible in Fig. 2, is 58 mm $\times$ 58 mm large, with a digital resolution of 17.7 px mm. The calibration is performed by acquiring static images of a plate situated in the FOV and equipped with millimeter paper from both cameras.

Data have been acquired at a sampling frequency of 2.7 kHz for 1 s, corresponding to approximately 300 cycles of vortex shedding from the upstream rod at $Re_d = 4.1 \times 10^4$. A LaVision high-speed controller ensures the synchronization between the acquisition of the images and the laser pulses.

In the processing phase of the raw images, performed with the commercial software *Davis 8.4* by LaVision, an interrogation window of 32 px $\times$ 32 px with 75% overlapping is employed. A mask is applied to neglect the region in the vicinity of the airfoil surface due to the high number of invalid points generated by the reflections, especially in the melamine configuration case. The mask also includes the shadow shed by the airfoil leading edge. Elsewhere, invalid points are either interpolated in time or reconstructed from adjacent points with the *smoothn* function by Garcia (2010), which is based on a penalized least squares method.

Furthermore, the time super-sampling algorithm by Scarano and Moore (2011) is used with a factor 3, leading to a final sampling frequency of 8.1 kHz. The super-sampling model is based on Taylor's frozen-turbulence approximation between two consecutive vector fields in time. The assumption is valid within timescales that are smaller than the flow-dissipation ones. This technique is suitable for investigating datasets where the dominant motion is aligned with the measurement plane. The resulting time step of the PIV measurements Δ_{Ts} is equal to $\Delta_{Ts} = \Delta_T / S_s$, where Δ_T is the original time separation between image couples and S_s is the super-sampling factor.

The maximum frequency that can be inspected is, however, limited by the low-pass filtering effect of PIV due to the averaging over the interrogation windows (Foucaut et al. 2004). The maximum frequency can be estimated by comparing the convection velocity with the resolution of the employed interrogation window. This aspect puts a

limitation on the size of turbulent eddies and the frequencies that can be analyzed, which may be below the Nyquist one. In the present case, the maximum frequency to avoid spurious results is estimated to be 0.9 kHz.

PIV uncertainty is made of random and systematic errors. The main sources of systematic errors in a PIV campaign are usually peak locking, particle slip, calibration errors, and limited spatial resolution. Peak locking is due to the tendency of calculating velocity towards integer displacements caused by situations in which the particle image size is smaller than the camera pixel. In the present experiments, the particle size at the indicated magnification factor is found to be about 0.5 px. In order to avoid peak-locking issues, de-focusing of the particles has been carried out to reach a $1.5 - 2$ px particle diameter in the camera sensor (Westerweel et al. 1997).

Particle slip (Melling 1997) is a physical effect linked to the inertia of the seeding particles that may experience a lag with the flow. It can be estimated as the response time τ_{slip} related to the tracer particle multiplied by the particle acceleration. Given the $\tau_{slip} \approx 0.5\,\mu$s of the employed seeding, this phenomenon is expected to provide a negligible contribution to the overall uncertainty.

Calibration errors arise from the third-order polynomial mapping function that is generated to relate the pixel dimension to a geometrical coordinate. In the present case, LaVision's self-calibration routine is applied to eliminate any potential misalignment in the original calibration. The uncertainty associated with the calibration errors is verified automatically with Davis 8.4 and corresponds to a residual error in the flow field of about 0.05 px.

The finite spatial resolution is linked to the transfer function of the PIV correlation algorithm for scales ranging from the FOV to the interrogation window. For the present study, this source of uncertainty is estimated following the approach of Schrijer and Scarano (2008). Since an iterative cross-correlation algorithm is employed, structures with 1 mm scale length can be reconstructed with a 68% confidence level.

Random errors are mainly due to the cross-correlation algorithm on which the PIV is based. Indeed, the cross-correlation analysis cannot provide an accurate representation of the stochastic nature of turbulence. An estimation of this error is based on the work of Westerweel (1997) and amounts to 0.1 px. Moreover, the convergence of statistic quantities depends on the number of uncorrelated data points that are processed. This aspect will be covered in greater detail in Sect. 3.2.1.

The overall systematic and random components of PIV uncertainty can be approximately determined with Davis 8.4. The built-in method is based on correlation statistics and evaluates the differences in the correlation peaks computed from a pair of interrogation windows that are mapped back onto each other (Wieneke 2015). The uncertainty is provided for individual instantaneous velocity vectors and is quantified through propagation techniques (Sciacchitano and Wieneke 2016). Results indicate a maximum uncertainty on the velocity of $0.05\,U_\infty$ in the streamwise component and $0.04\,U_\infty$ in the upwash one at $Re_d = 4.1 \times 10^4$. Similar values are retrieved also at $Re_d = 2.7 \times 10^4$ and $Re_d = 5.4 \times 10^4$.

2.3 POD analysis

2.3.1 Algorithm description

The POD is a data-driven decomposition designed to provide an optimal approximation of a given dataset. This technique allows for the extraction of a set of orthogonal bases from a typical eigenvalue problem. The bases are modes that can be ordered by energy content. In this work, the POD is employed with the aim to determine which turbulence scales play a major role in terms of flow field alterations by the porosity. The choice of this method over other techniques, such as Fourier analysis, is driven by the fact that its optimal decomposition minimizes the error of reconstruction of the largest scales of turbulence (Cenedese et al. 1997), which are the most relevant and visible in a rod–airfoil configuration (Jacob et al. 2005).

It is out of the scope of the paper to exhaustively describe the POD algorithm, for which the interested reader should refer to Ninni and Mendez (2020) and the extensive tutorials recorded by the authors and available online. A brief summary of the method is reported hereafter. The initial step of the decomposition is the arrangement of a sequence of PIV snapshots into a matrix $\boldsymbol{D}$:

$$\boldsymbol{D} = \begin{bmatrix} u_0(0) & \dots & u_0(t_k) & \dots & u_0(t_n) \\ \vdots & \ddots & \vdots & \ddots & \vdots \\ u_{n_s}(0) & \dots & u_{n_s}(t_k) & \dots & u_{n_s}(t_n) \\ v_0(0) & \dots & v_0(t_k) & \dots & v_0(t_n) \\ \vdots & \ddots & \vdots & \ddots & \vdots \\ v_{n_s}(0) & \dots & v_{n_s}(t_k) & \dots & v_{n_s}(t_n) \\ \omega_0(0) & \dots & \omega_0(t_k) & \dots & \omega_0(t_n) \\ \vdots & \ddots & \vdots & \ddots & \vdots \\ \omega_{n_s}(0) & \dots & \omega_{n_s}(t_k) & \dots & \omega_{n_s}(t_n) \end{bmatrix} \quad (1)$$

Data in the spatial domain are stored in the rows, while time is discretized along the columns. The matrix is built so that the horizontal and vertical velocity components are stacked, as well as vorticity $\vec{\omega}$, along each column. The addition of vorticity is made to mitigate the occurrence of coupled modes that are typical of POD applications for a rod–airfoil configuration.

Before feeding $\boldsymbol{D}$ to the POD algorithm, its mean along the rows (in time) is subtracted from all columns. Vorticity

$\vec{\omega} = \vec{\nabla} \times \vec{U}$ has been computed directly from the velocities using a second-order central difference scheme and a first-order backward and forward schemes at the boundaries of the FOV (Bingham et al. 2018).

A general factorization of D is

$$D = \phi \Sigma \psi^T, \tag{2}$$

where the matrices ϕ and ψ contain the spatial and temporal structures, respectively. Σ is diagonal and represents the energy content of each mode. The POD algorithm allows for the optimization of the temporal basis that minimizes the approximation error. This is achieved by decomposing a dataset with regard to the energy content of the different modes.

The optimization can be performed with the method of Lagrangian multipliers, which leads to an eigenvalue problem for the temporal correlation matrix $K = D^{\dagger}D$. An eigenvalue decomposition for K can be written as $K = \psi \Sigma^2 \psi^T$, where Σ is a diagonal matrix made by the square root of the eigenvalues of K, representing the energy of the modes, and ψ is made of the eigenvectors of K. From D, Σ, and Ψ, it is then possible to obtain the spatial basis Φ from Eq. 2.

2.3.2 POD as a spatial filter for turbulence

A broad range of turbulent scales is involved in the interaction between the airfoil and the wake of the upstream circular cylinder. The vortices periodically shed by the rod represent the largest scales. However, smaller scales are also convected downstream according to the energy cascade phenomenon (Pope 2000). The POD can be used as a spatial filter to distinguish the different turbulence scales that interact with the airfoil by decomposing the flow with regard to the energy content of its modes. This particular application of the algorithm as a length filter is effective in a rod–airfoil configuration due to the presence of few dominant modes with high energy content (Jacob et al. 2005). In fact, this particular feature is expected to ensure accurate isolation of the convection of a range of flow structures.

This assumption can be verified in Fig. 3, which presents the energy content of the POD modes for the solid, the porous, and the melamine case. The values are computed from the eigenvalue problem of the temporal correlation matrices generated by a dataset at $Re_d = 4.1 \times 10^4$. In the plot, each modal energy has been divided by the total one, calculated by summing the energies of all modes up to the cutoff mode.

The result clearly indicates that four initial modes combined account for almost 40% of the total energy of the flow in all the considered cases, in agreement with the results of Jacob et al. (2005). These are related to the largest scales of turbulence shed by the rod.
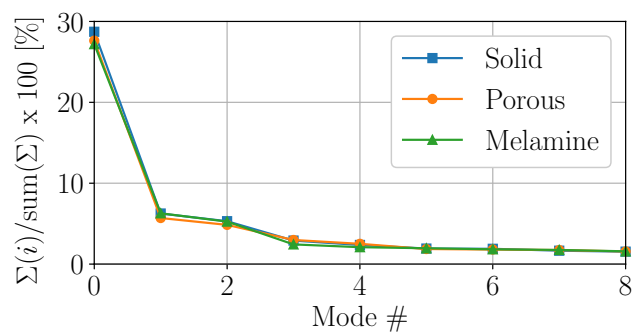

Fig. 3 Energy content of different modes obtained from a POD of the flow. The *y*-axis indicates the percentage of the total energy

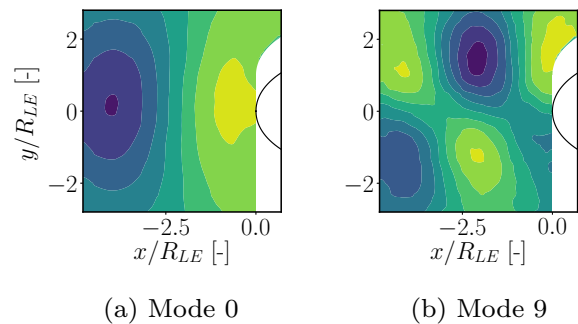(a) Mode 0   (b) Mode 9

Fig. 4 Modes obtained from POD decomposition of the upwash component of velocity in proximity of the solid airfoil for $Re_d = 4.1 \times 10^4$

To provide a visual representation of this statement, mode 0 and mode 9 for the upwash velocity component for $Re_d = 4.1 \times 10^4$ are plotted in Fig. 4a, b, respectively.

Mode 0 appears to be characteristic of the vortex-shedding phenomenon, which accounts for the highest energy content in the spectrum of temporal structures. When lower energy modes are considered, such as mode 9, the coherent turbulent structures are visibly smaller. Overall, the algorithm allows isolating one or more structures of the same size with each POD mode.

An additional way to visualize the filtering role of POD with turbulence is to plot the local velocity spectra of flow recompositions obtained from groups of POD modes (i.e., energy bins). Figure 5 presents the PSD of the upwash component of velocity evaluated on the stagnation streamline at 2 radii of curvature of the leading edge from the stagnation point. These are computed with the Welch method (Welch 1967) applied with a window size of 2^9 sampling elements and a frequency resolution of 15.8 Hz.

A notable result in this figure is that the spectrum corresponding to the most energetic recomposition has a strong peak at the vortex-shedding frequency, differently from the other two spectra. Furthermore, when lower energy modes are considered, i.e., $50 - 70\%$ or $70 - 90\%$, frequency ranges
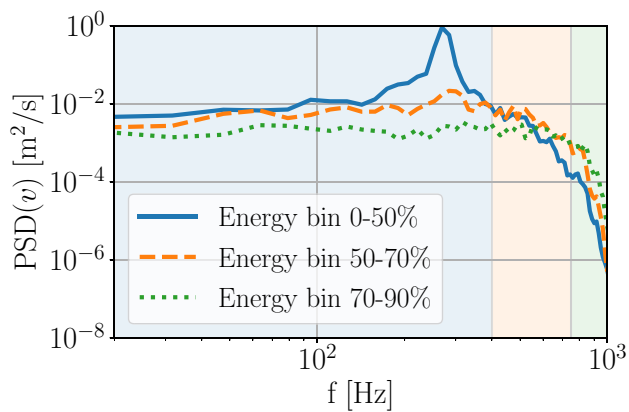
Fig. 5 Local spectra of upwash velocity extracted at 2 radii of curvature of the leading edge from the stagnation point for the different modal recompositions of the flow following a POD analysis

where each energy bin is predominant over the others can be clearly identified. These are filled with uniform colors in Fig. 5 and can be seen as the ranges of turbulence scales that are band filtered by the recomposition of the considered bin. In Sect. 3.3, the results of the application of POD will be presented for acquisitions of 0.5 s, corresponding to 150 cycles of vortex shedding.

3 Results

3.1 Far-Field noise results

The aeroacoustic spectra averaged over the 64 microphones of the array are presented in Fig. 6. The Strouhal number is based on the rod-diameter and the free-stream velocity of the flow. The region in the plot that is marked in grey indicates the St-range at which the noise coming from the rod dominates over the solid airfoil noise.

For all the considered velocities, the maximum sound-pressure level occurs at the vortex-shedding frequency, corresponding to a Strouhal number $St \approx 0.2$. This is expected in a rod–airfoil configuration (Jacob et al. 2005). In general, L_p grows along with the Reynolds number in the whole frequency range. The effect of porosity is to reduce noise at low frequencies and to increase it at high frequencies with respect to the solid case.

In order to better visualize the effects of the different airfoil configurations, the relative sound-pressure levels ΔL_p with reference to the solid case are evaluated. With this convention, a positive ΔL_p indicates a noise reduction, whereas a negative ΔL_p denotes noise increase. Figure 7 presents the far-field results obtained at different rod-based Reynolds numbers.
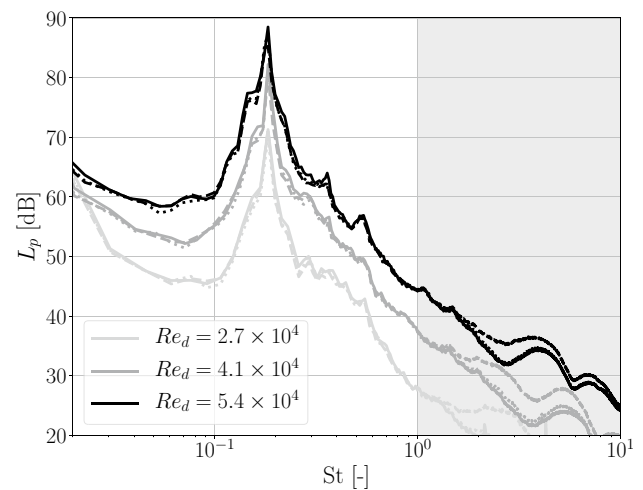

Fig. 6 Sound-pressure level spectra of the airfoil configurations for different rod-based Reynolds numbers. Solid ▬▬; porous ▪ ▪ ▪; melamine ▪▪▪▪▪. The data are acquired at 1 m from the airfoil with a reference pressure of $p_{\mathrm{ref}} = 20\,\mu\mathrm{Pa}$ and are averaged over the 64 microphones of the array

The spectra related to the porous airfoil configuration feature a noise increase up to about $St = 0.15$ that is attenuated in the case of the melamine airfoil, especially for higher velocities. Above this threshold, the porous treatments effectively reduce both tonal and broadband noise components, with a maximum abatement of about 2 dB. The mitigation is generally more pronounced around the vortex-shedding peak at $St = 0.18$ and gradually decreases up to $St = 1$, where the porous spectra start converging with the solid one. This result agrees with the acoustic beamforming measurements performed by Zamponi et al. (2020).

On the contrary, a notable negative ΔL_p for both porous and melamine airfoils is found at higher frequencies, consistently with results previously obtained (Zamponi et al. 2019). The origin of this noise regeneration for the melamine airfoil is attributable to the more substantial surface roughness of the foam. Indeed, the role played by surface roughness noise (Howe 1991; Liu et al. 2006, 2007) is more significant for materials characterized by low values of static resistivity due to the typically larger dimensions of the pores (Geyer et al. 2010). However, this mechanism cannot be directly transposed to the porous airfoil configuration since the presence of the woven wire mesh ensures the same surface roughness as the solid baseline. A possible explanation for the noise increase may come from the fluid–structure interaction between the flow and the hard-plastic exoskeleton, as suggested by the characterization of the boundary layer around the airfoil performed by Zamponi et al. (2019).

Moreover, the sudden transition occurring at $St = 0.18$ can be readily explained by a slight shift of the vortex-shedding peak due to the higher blockage effect given by the
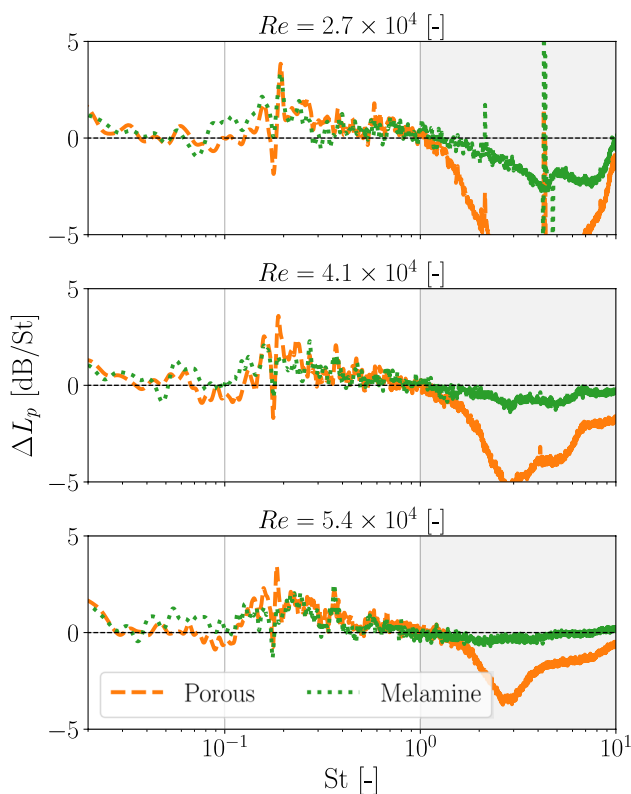
$Re = 2.7 \times 10^4$ [-]

$Re = 4.1 \times 10^4$ [-]

$Re = 5.4 \times 10^4$ [-]

ΔL_p [dB/St]

- - - Porous   ······ Melamine

St [-]

Fig. 7 Sound-pressure level spectra of the porous and the melamine airfoil configuration relative to the solid one for different rod-based Reynolds numbers. The data are acquired at 1 m from the airfoil with a reference pressure of $p_{\text{ref}} = 20\,\mu$Pa and are averaged over the 64 microphones of the array

porous treatment of the airfoil. This evidence is supported by the data listed in Table 2, which reports the sound-pressure level $L_{p,\text{VS}}$ and the Strouhal number St_{VS} corresponding to the vortex-shedding peak in the spectra of Fig. 7. The first conclusion that can be drawn from the analysis of the tonal noise is that the porous treatments of the airfoil decrease the level of the vortex-shedding peak by approximately 1.5 dB for each rod-based Reynolds number, with no significant impact of the exoskeleton. The second conclusion is that the presence of the airfoil reduces St_{VS} by about 4%, most probably due to the higher blockage effect. As previously mentioned, also the porous treatments of the airfoil contribute to the decrease of the Strouhal number at which the vortex

shedding occurs. Interestingly, this effect is more important for the porous airfoil configuration for every rod-based Reynolds number considered, hinting at a possible increased blockage generated by the hard-plastic exoskeleton.

3.2 Flow-field visualization results

3.2.1 Mean velocity fields

The PIV mean velocity fields related to the streamwise u and upwash v velocity component are illustrated in Fig. 8a, b, respectively. The datasets have been undersampled at 200 Hz in order to ensure uncorrelated data points.

The main effect of porosity on the mean velocity is to mitigate the acceleration of the upwash mean velocity component observed in the solid case in the region of higher curvature of the airfoil. This can be explained by flow penetration within the melamine foam. For the streamwise component, all the airfoil configurations feature a similar trend with the only exception of a little region near the stagnation point, where the flow penetration yields higher values in the porous and the melamine case with respect to the solid one. The results are in agreement with the LES computations presented by Zamponi et al. (2020).

3.2.2 Turbulence quantities and Reynolds number dependency

Turbulence intensity is defined as the root mean square of the streamwise u' and upwash v' velocity fluctuations normalized by the free-stream velocity, while the turbulent kinetic energy (TKE) is defined as

$$\text{TKE} = \frac{1}{2}\left[\overline{(u'/U_\infty)^2} + \overline{(v'/U_\infty)^2}\right].\qquad(3)$$

The turbulence intensity fields evaluated for $Re_d = 4.1 \times 10^4$ are shown in Fig. 9.

The effects of porosity on turbulence can be better quantified by extracting the results in Fig. 9 along the stagnation streamline. These are reported in Fig. 10. In this case, the effects of varying the Re_d are also included in the analysis.

Both streamwise and upwash velocity components feature a maximum in the upstream region due to the strong turbulence shed by the rod. The decrease of u' in the solid

Table 2 Sound-pressure level $L_{p,\text{VS}}$ and Strouhal number St_{VS} characterizing the vortex-shedding peak in the acoustic frequency spectra for the different rod-based Reynolds numbers and the different airfoil configurations

Case	$Re_d = 2.7 \times 10^4$		$Re_d = 4.1 \times 10^4$		$Re_d = 5.4 \times 10^4$	
	$L_{p,\text{VS}}$ [dB]	St_{VS} [-]	$L_{p,\text{VS}}$ [dB]	St_{VS} [-]	$L_{p,\text{VS}}$ [dB]	St_{VS} [-]
Solid	72.4	0.186	82.2	0.184	89.1	0.182
Porous	71.1	0.184	80.8	0.182	87.4	0.180
Melamine	70.9	0.185	81.1	0.183	87.7	0.181
Rod	68.6	0.193	79.8	0.192	84.7	0.190

(a) Streamwise velocity component $\bar{u}/U_\infty$

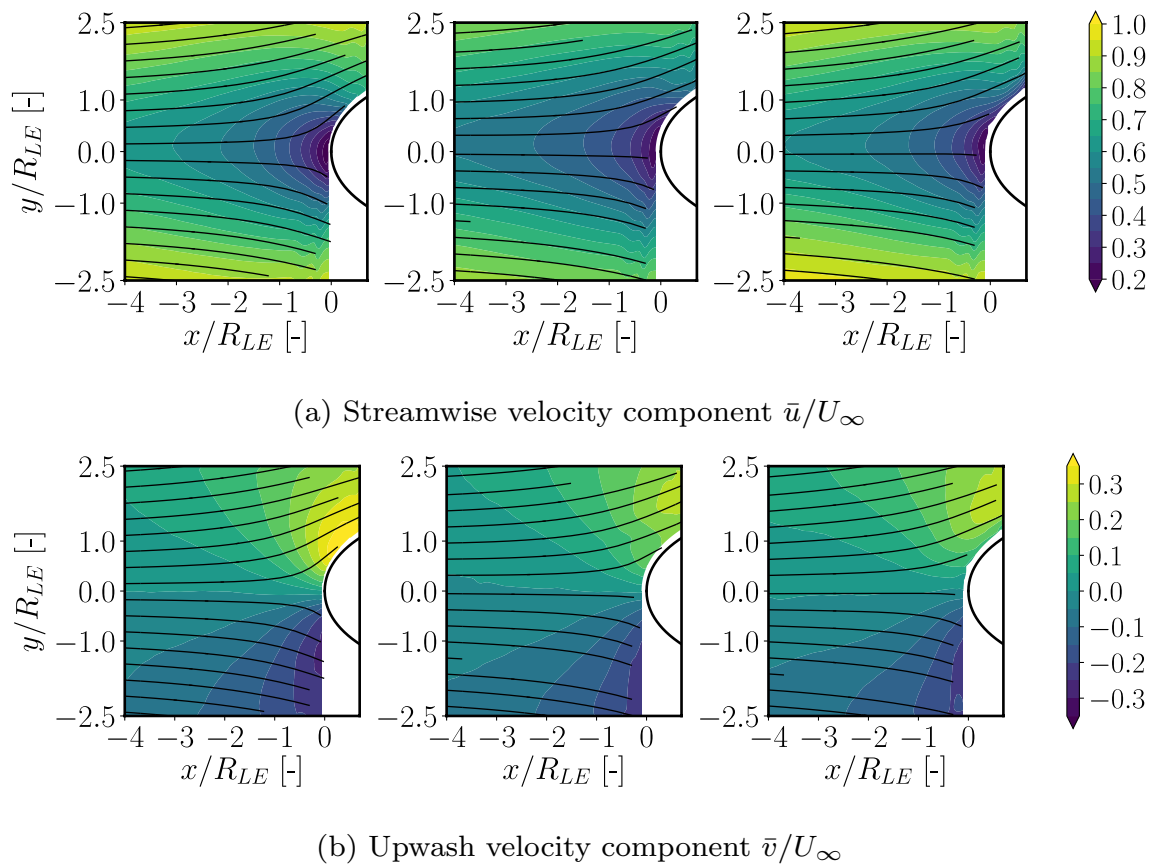(b) Upwash velocity component $\bar{v}/U_\infty$

Fig. 8 Uncorrelated mean velocity fields from PIV measurements for $Re_d = 4.1 \times 10^4$. From left to right: solid, porous, and melamine case

case is mitigated near the leading edge due to the flow penetration that reduces the transfer of momentum occurring between the two velocity components. This effect is caused by the blockage effect of the airfoil (Zamponi et al. 2020) and results in a strong attenuation of v' by the porous treatments in the stagnation region relatively to the solid model. The absence of the permeable exoskeleton in the melamine airfoil enhances this effect, leading to lower values of v' in the stagnation region.

The effect of the rod-based Reynolds number is to extend the region where porosity has an impact on the turbulent field. In particular, the location from which porosity starts affecting the trends of u' and v' moves upstream (i.e., at lower x/R_{LE}) with increasing Re_d. Moreover, the effects of porosity on the velocity fluctuations are magnified at higher values of Re_d with reference to the solid case, especially for the upwash component, as visible in Fig. 10b. In agreement with Zamponi et al. (2020), the decrease in turbulence intensity in the upwash component due to porosity is predominant over the minor increase in the streamwise component. Therefore, a reduction in TKE is expected. This is confirmed in Fig. 10c, where it is possible to observe that TKE decreases in the stagnation region for all the considered

cases, with more significant reductions obtained with the melamine airfoil.

The dependence of the turbulent-field alterations due to porosity on the Reynolds number observed in the PIV measurements in Fig. 10 can be further investigated by evaluating the turbulent velocity spectrum at a location near the airfoil. Figure 11 depicts the PSD of the upwash component of the velocity fluctuations computed at $(x, y)/R_{LE} = (-0.25, 0)$ for the three airfoil configurations and the different Re_d. The PSDs are computed using the Welch method (Welch 1967) with a window size of 2^9 sampling elements and a frequency resolution of 15.8 Hz.

For all the PSDs, the vortex-shedding frequency peak occurs at $St \approx 0.18$, in agreement with the far-field acoustic spectra presented in Sect. 3.1. The effect of porosity is confined to the low-St range of the velocity PSDs, with a frequency extent and amplitude that increase along with the Reynolds number. The presence of the permeable exoskeleton does not appear to alter the magnitude of the reduction in P_{vv} near the vortex-shedding frequency peak but has an impact at lower Strouhal numbers. This trend is particularly visible at $Re_d = 2.7 \times 10^4$, for which the spectrum related to the porous case starts converging with that of the solid
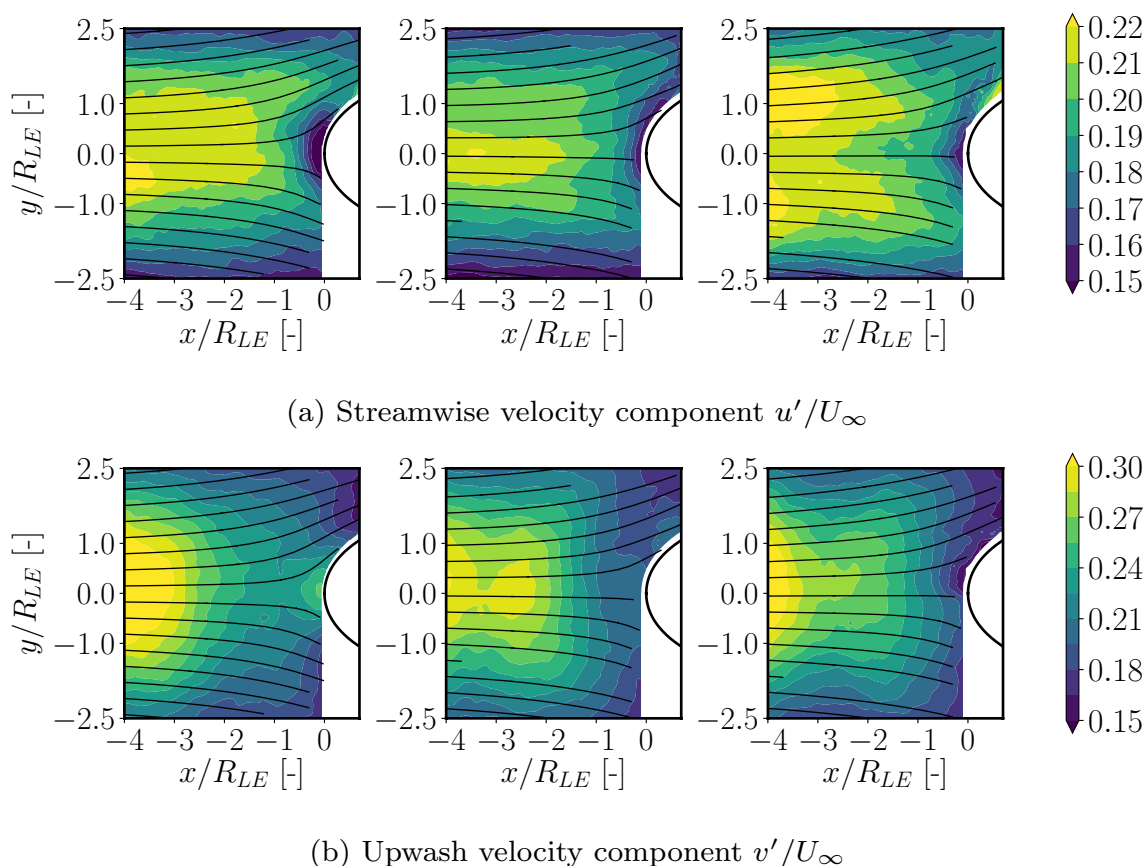
(a) Streamwise velocity component u'/U_∞

(b) Upwash velocity component v'/U_∞

Fig. 9 Turbulence intensity fields from PIV measurements for $Re_d = 4.1 \times 10^4$. From left to right: solid, porous, and melamine case

airfoil for $St < 0.03$, differently from the spectrum of the melamine configuration that remains constant. The present low-frequency deviation between the porous and the melamine case may partly explain the difference in the upwash turbulence intensity observed in Fig. 10.

3.3 POD results

The results presented in this section are related to $Re_d = 4.1 \times 10^4$. The first analysis that has been performed is on the choice of the appropriate number of modes that should be considered to reconstruct a dataset. Generally, low energy modes tend to corrupt flow reconstructions with erroneous velocity vectors that are due to the random error component of PIV. Raiola et al. (2015) proposed a method to determine the cutoff mode required to reconstruct the flow without the random noise coming from PIV measurements. The criterion used in the present work is based on a simplified version of the above-mentioned one that has been validated against other methods by Brindise and Vlachos

(2017). This method defines the cutoff mode k^* as the first mode for which

$$\frac{\lambda_{k^*}}{\lambda_{k^*-1}} \geq 0.999, \tag{4}$$

where λ denotes the eigenvalues of the decomposition. The application of this method to the investigated dataset yields the cutoff at mode 156 for the solid case (56% of total energy) and at mode 162 for the other cases (56% of total energy for porous case and 55% for the melamine one).

In addition, a recomposition strategy must be defined in order to compare the different airfoil configurations. The adopted methodology is based on the approach followed by Tandalam et al. (2010) that considers the energetic content of the modes, computed from the eigenvalues of the temporal correlation matrix K. The significant modes for each case are grouped to obtain equal energy bins. A visual representation of the applied strategy is shown in Fig. 12 for the energy bins 0-50%, 50-70%, 70-90%, and 90-99.9%.

3.3.1 Characterization of inflow conditions

The comparison of the different airfoil configurations is legitimate if the POD recompositions related to the different energy bins are characterized by comparable turbulence scales and inflow conditions. This assumption can be verified through a two-dimensional Fourier analysis of the most upstream flow region of the available FOV. A squared window centered in $(x, y) = (-3, 0) R_{LE}$ with side length of $2.7 R_{LE}$ is considered. The present window size is chosen to inspect turbulence scales that are of the order of the rod diameter. In particular, scales up to $1.3 d$ can be studied.
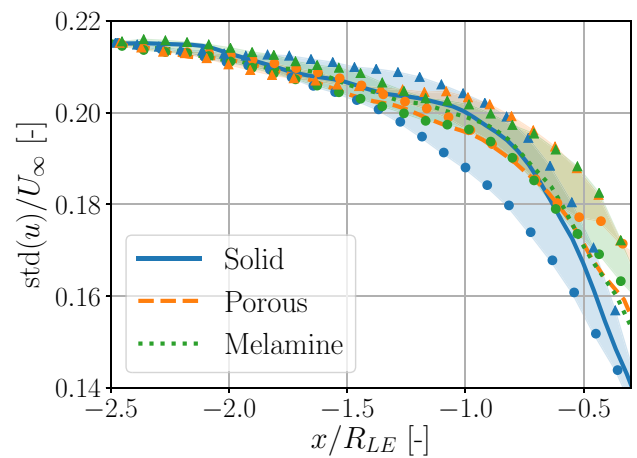
A spatial fast Fourier transform on the instantaneous velocity field inside the window is performed and multiplied by its complex conjugate to obtain a PSD. The procedure is repeated for all snapshots, and the results are then averaged. The variance of the snapshots is checked in order to ensure that the averaging procedure is not biased by one exceptional entry of the mean. The results for the streamwise and upwash components are shown in Fig. 13 for the solid, the porous, and the melamine airfoil configuration and for all the energy bins. A general good agreement of the spectra is found in this case, although minor deviations occur for the most energetic reconstruction of the streamwise component, which may be due to the higher uncertainty compared to the upwash one. Overall, the good match of the contour curves indicates that inflow conditions obtained with the POD reconstruction are comparable, making it feasible to perform the following analysis. Moreover, an estimation of the integral length scales of turbulence Λ_x corresponding to each energy bin is shown in Fig. 14.

The computation of Λ_x is carried out by integrating the spatial correlation coefficient R_u as shown in Equation 5
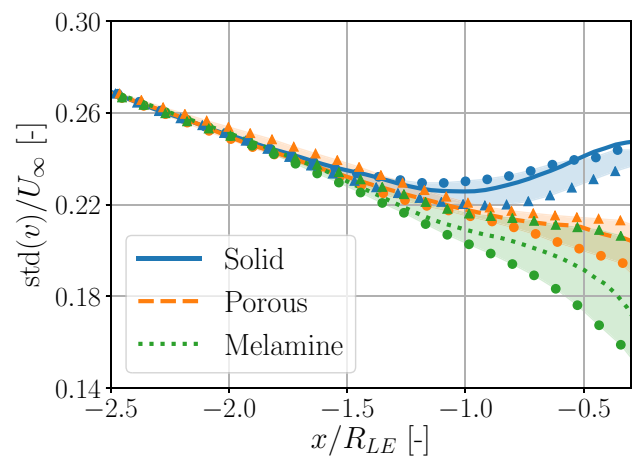
$$\Lambda_x = \int_0^{X^*} R_u \, dx \tag{5}$$

with $\quad R_u = \dfrac{\overline{u'(x)u'(x+r)}}{\sqrt{\overline{u'^2(x)}}\sqrt{\overline{u'^2(x+r)}}}, \tag{6}$
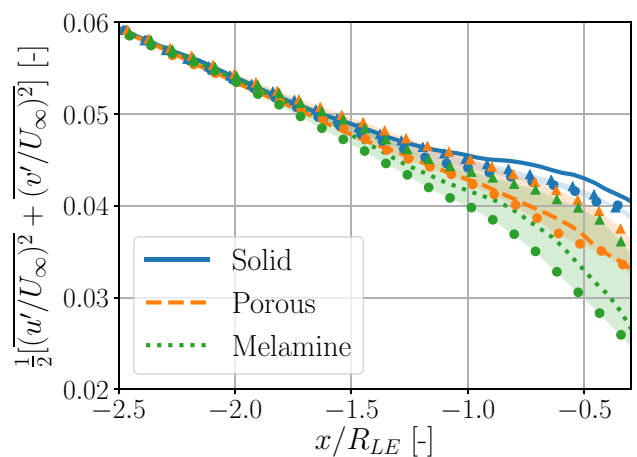
where x is the streamwise coordinate. The integration procedure is performed numerically by truncating the correlation functions at the first root X^*, i.e., $R_u(X^*) = 0$.

(a) Streamwise turbulence intensity
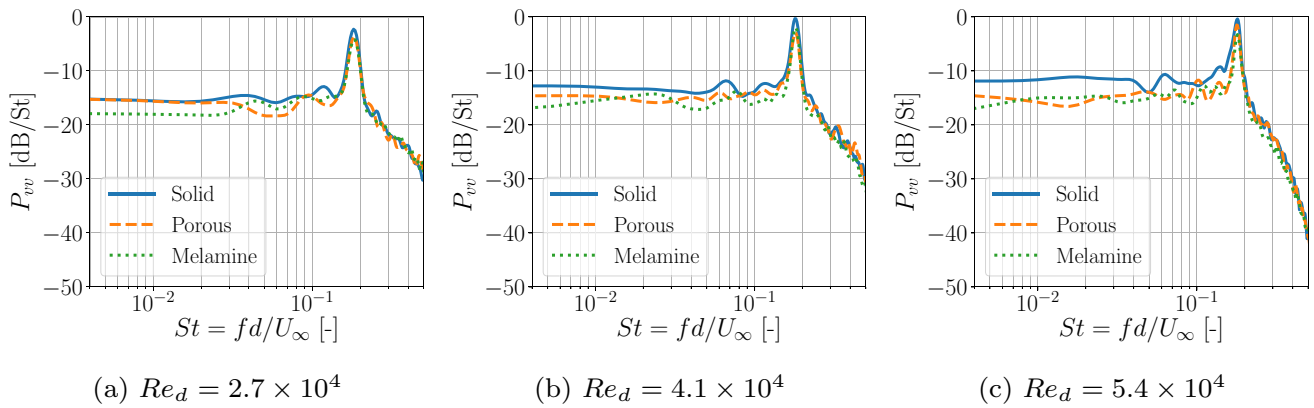
(b) Upwash turbulence intensity

(c) TKE

(a) $Re_d = 2.7 \times 10^4$ (b) $Re_d = 4.1 \times 10^4$ (c) $Re_d = 5.4 \times 10^4$

Fig. 11 PSD of the upwash component of the velocity fluctuations for the solid, porous, and melamine airfoil models from the PIV measurements at $(x, y)/R_{LE} = (-0.25, 0)$. The reference is $1\,\mathrm{m^2\,s^{-1}}$
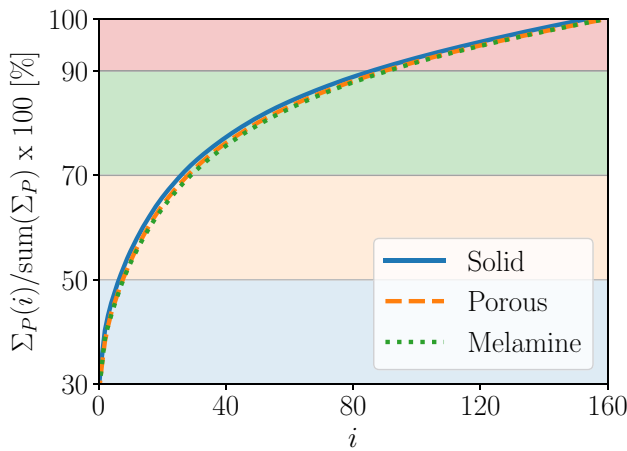

Fig. 12 Cumulative sum of the energy content of each mode i. Only the modes below to the cutoff are considered. The ranges used to recompose the flow are highlighted with different colors

Nevertheless, the limited extension of the FOV considered in the PIV measurements makes it difficult to reach convergence in these functions, especially for the $0 - 50\%$ energy bin. In this case, the length scale has been estimated by dividing the convection velocity by a local timescale. Therefore, the results presented in Fig. 14 constitute a conservative estimation of the actual integral length scale and confirm what is observed in Fig. 5 about the correspondence between the most energetic decomposition of the flow and the inclusion of the largest turbulence scales. Furthermore, the different airfoil configurations feature comparable values for each energy bin, in agreement with the results shown in Fig. 13. The first energy bin $0 - 50\%$ is representative of scales on the order of the rod diameter and of the radius of curvature of the leading edge.

3.3.2 Turbulence analysis

A qualitative estimation of the distortion experienced by the coherent structures in the interaction with the airfoil surface can be obtained with the POD recomposition. A useful tool to identify vortical structures is the Γ_2 function, which is based on the normalized angular momentum of the velocity field, following the definition given by Graftieaux et al. (2001). Figure 15 presents a comparison of the instantaneous fields of the Γ_2 function alongside the velocity fields for the solid and the melamine airfoils. The data have been reconstructed using the most energetic POD energy bin in order to isolate the largest turbulence structures. The generic time step $t_1 = 0$ in Fig. 15a, c has been chosen to ensure approximately the same inflow conditions, i.e., a coherent structure that is convected towards the leading edge of the airfoil. The second snapshots in Fig. 15b, d are taken at $t_2 \approx 2.2\,d/U_\infty$ and correspond to a scenario in which the coherent structure is interacting with the airfoil.

From the comparison of the final time steps t_2 for the solid and the melamine airfoil, it appears that two different deformation mechanisms of the turbulent structure take place at the leading edge. In particular, the solid surface tends to break up the incoming vortical structure, whereas the presence of the melamine foam seems to allow for a smoother distortion of it. The present evidence is consistent with the flow-field results for which porosity reduces the acceleration of the upwash velocity component in the higher curvature region of the airfoil with respect to the solid configuration. These trends have been also observed for other coherent structures at different time steps, which are not reported in the manuscript for reasons of brevity.

A more in-depth analysis of the impact of porosity on the turbulent flow can be carried out by investigating how the
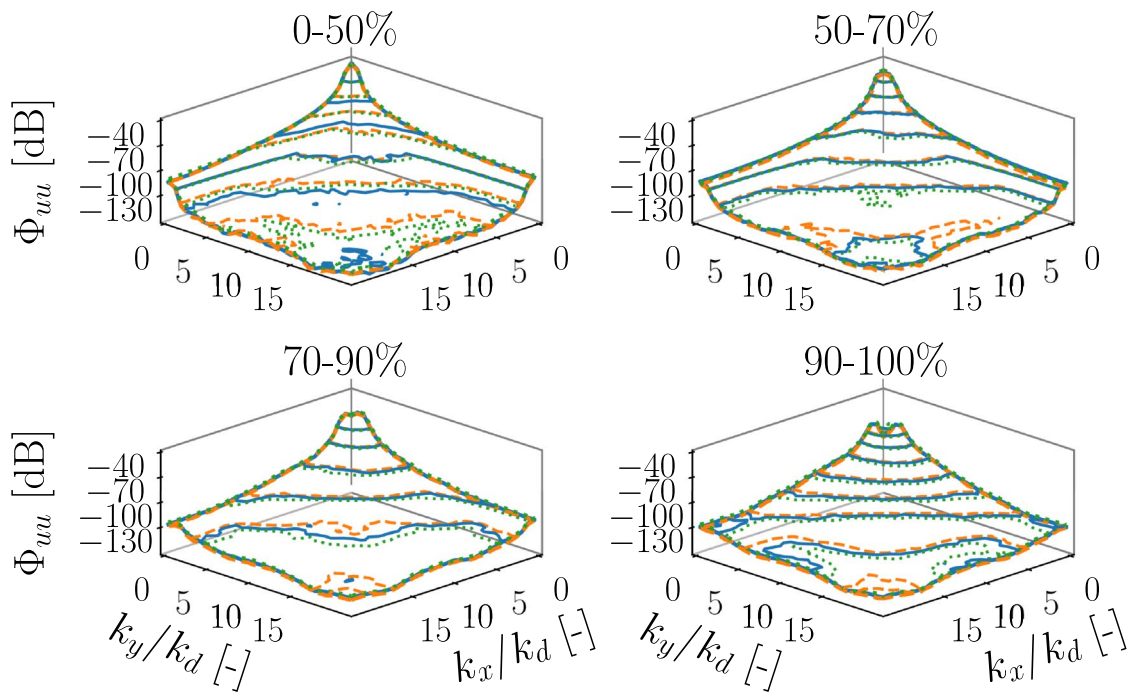
(a) Streamwise velocity component
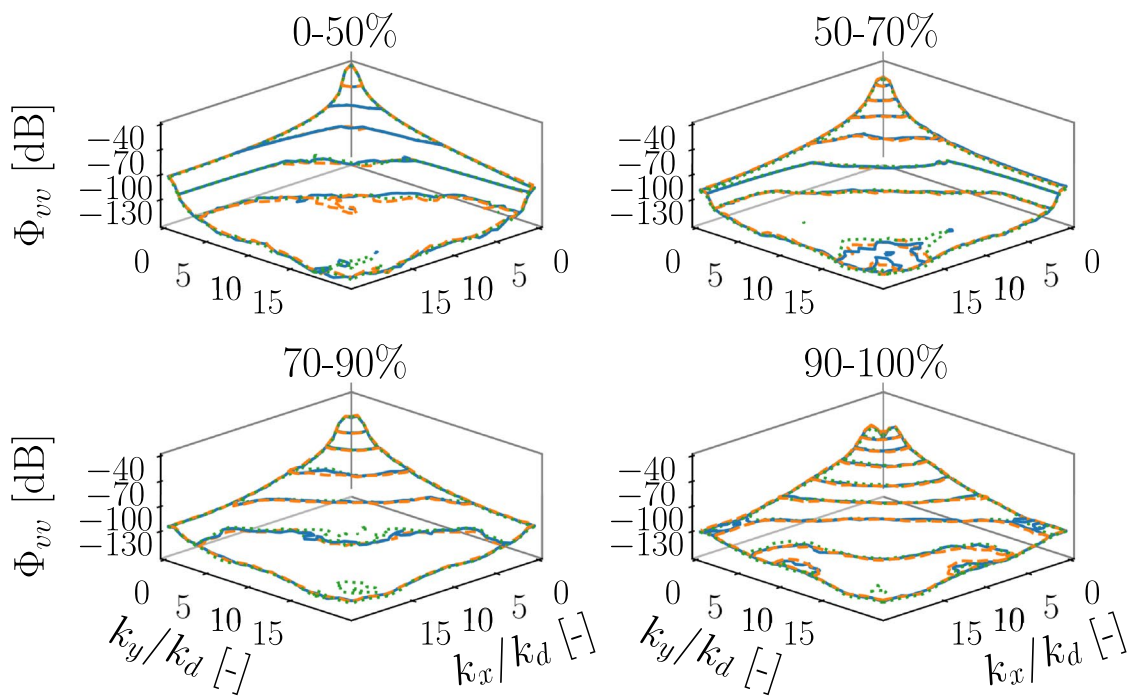
(b) Upwash velocity component

Fig. 13 Two-dimensional PSD computed for different airfoil configurations (Solid: ——; Porous: - - -; Melamine: ·····) and four POD recompositions. The *x*- and *y*-axes are non-dimensionalized with the wavenumber relative to the rod diameter. The reference is $1\,\mathrm{m^4s^{-2}}$
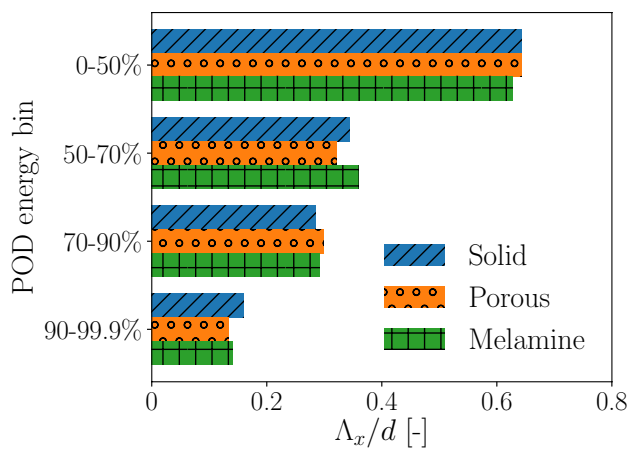
Fig. 14 Estimation of the integral length scales of turbulence obtained with the proposed POD spatial filter and non-dimensionalized with the rod diameter d

different turbulence scales are affected. Figure 16 presents the results for the turbulent quantities along the stagnation streamline for the three airfoil configurations and the four energy bins. The streamwise component of turbulence intensity in Fig. 16a features magnitudes and trends that coincide for the different airfoil configurations and for all energy bins of the POD. Slight differences in the upstream region for the $0 - 50\%$ and $50 - 70\%$ bins are expected from the analysis of the inflow region shown in Fig. 13. In the $50 - 70\%$ energy bin, strong oscillations are observed for the porous and the melamine case that could be due to the pulsation of coherent structures.

The upwash component in Fig. 16b clearly shows that the trends previously reported in Fig. 10b are fully captured by the most energetic modes, whereas no significant impact of porosity is found in the other energy bins. In general, all quantities shown in Fig. 16 drop according to the energy content of the bin that is considered to reconstruct the flow. Also in the case of TKE, the main trends of the turbulence statistics in Fig. 10c concerning the impact of porosity on the turbulence distortion are included entirely in the most energetic modes, which are linked to length scales of turbulence on the order of the rod diameter. Conversely, lower energy modal reconstructions exhibit similar values for all the airfoil configurations.

Finally, a spectral analysis is performed on the upwash velocity component, which plays an important role on the far-field noise according to Amiet's theory (Amiet 1976). In order to compare the different configurations, Fig. 17 presents the relative local spectra of this velocity component ΔP_{vv} with reference to the solid model. The spectra have been obtained by averaging three measurement points along the stagnation streamline, centered around $(x, y)/R_{LE} = (-3, 0)$ and $(x, y)/R_{LE} = (-0.25, 0)$.

Similarly to the far-field aeroacoustic measurements in Fig. 7, a positive ΔP_{vv} indicates a reduction in the PSD. The location at $x/R_{LE} = -0.25$ is chosen as a trade-off between the enhancement of the porosity effects and the avoidance of invalid PIV data points that are reconstructed due to reflections. Concerning the latter aspect, the number of valid points obtained at $x/R_{LE} = -0.25$ is above 80% for each airfoil configuration. The remaining ones are either interpolated in time or reconstructed. Results are also reported at the upstream location $x/R_{LE} = -3$, where the effects of porosity are absent and ΔP_{vv} is expected to be zero. This is shown to assess the consistency of the methodology and ensure that any effect occurring in the stagnation region is due to porosity.

A significant influence of porosity can be observed in the stagnation region for the most energetic decomposition. Consistently with the trend of the turbulence intensity in Fig. 10, the melamine airfoil configuration is more effective in mitigating P_{vv} than the porous one, with reductions of up to 6.5 dB/St for the former and of 3.5 dB/St for the latter. For the porous airfoil, the positive ΔP_{vv} is seen only for the first decomposition, whereas in the melamine case the effect extends also to the energy bin 50-70%. For further decompositions, ΔP_{vv} drops to zero.

3.4 Discussion

The results presented above put the focus on the turbulent scales on the order of the rod diameter as those responsible for the aerodynamic effects observed in the stagnation region of the porous airfoil models. In particular, it appears that a weaker turbulence distortion takes place in correspondence with a porous leading edge, which constitutes a reduced geometrical discontinuity with respect to a solid wall. This also allows explaining why the impact of porosity on the PSD of the upwash turbulent velocity component in Fig. 11 is confined to the low-St range. The present trend is in line with the results of the aeroacoustic analysis, which indicate that the most appreciable noise mitigation is achieved at the vortex-shedding frequency peak. In addition, no notable differences in the noise emissions between the porous and the melamine airfoil configurations are found in the St-range $0.2 - 1$, similarly to what is observed for the upwash turbulent velocity spectra in Figs. 11 and 17.

These similarities suggest a potential link between attenuation in turbulence distortion and noise reduction and are consistent with the conclusions drawn by Zamponi et al. (2021) using the rapid distortion theory. As stated in this study, a better understanding of the turbulence–porous structure interaction and, specifically, of the alteration of the two-dimensional energy spectrum of the upwash turbulent velocity may lead to the elaboration of a novel noise-mitigation predictive model for porous airfoils based on Amiet's theory.
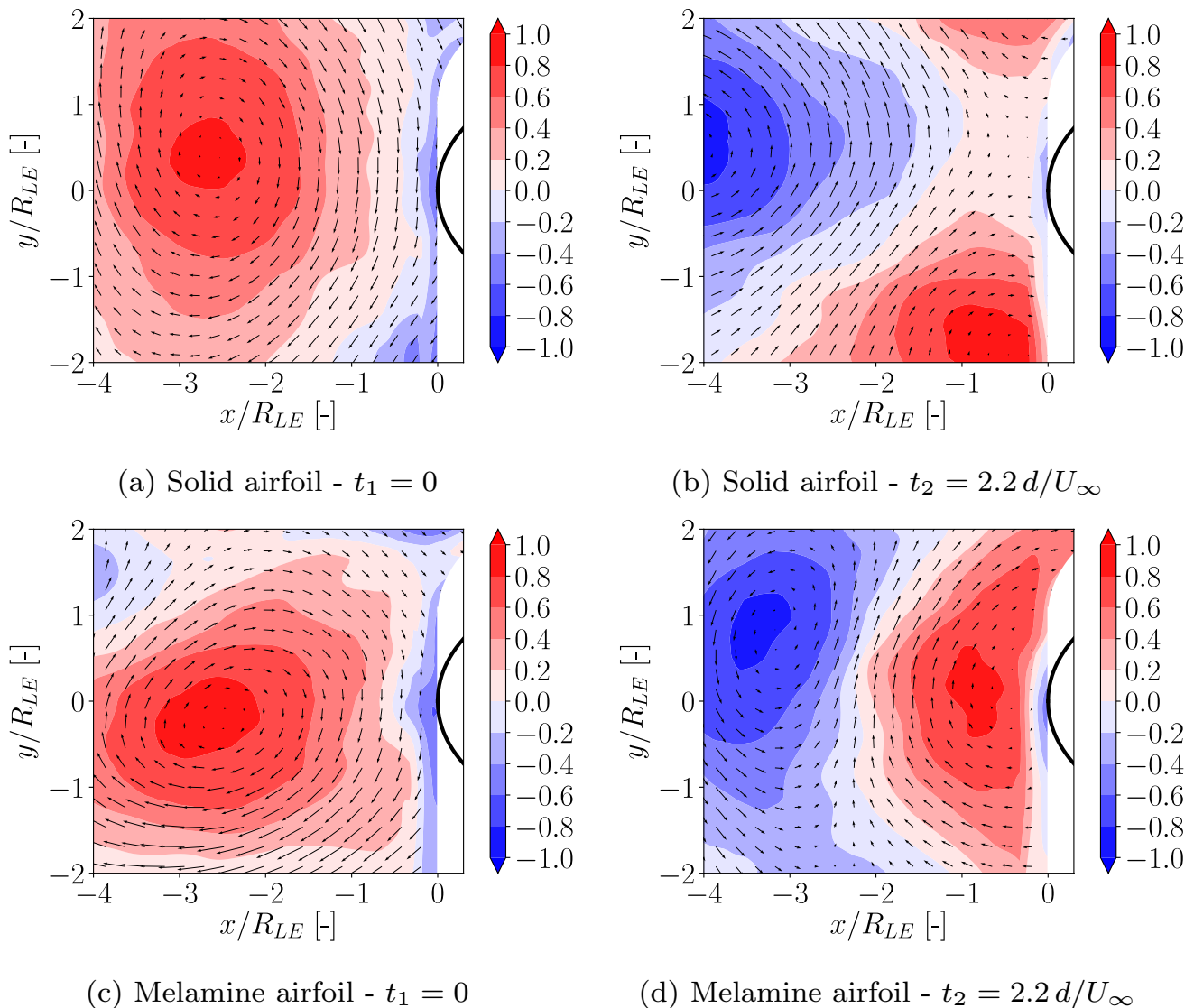
(a) Solid airfoil - $t_1 = 0$

(b) Solid airfoil - $t_2 = 2.2\,d/U_\infty$

(c) Melamine airfoil - $t_1 = 0$

(d) Melamine airfoil - $t_2 = 2.2\,d/U_\infty$

Fig. 15 Instantaneous Γ_2 and velocity fields reconstructed with the $0-50\%$ POD energy bin for the solid and melamine airfoil models. 14×14 measurement points have been considered in the computation of the function

However, the definitive connection between modification of flow-field characteristics and noise abatement has still to be established. Future investigations on the effect of porosity on the surface pressure fluctuations induced by turbulence interaction could be instrumental in achieving this objective.

4 Conclusions

The turbulent flow around solid and porous airfoils immersed in the wake of an upstream cylindrical rod and the relative noise emissions are investigated through time-resolved PIV and far-field microphone measurements for different Reynolds numbers. The results for a porous NACA-0024 profile equipped with a hard-plastic exoskeleton fitted with melamine foam (denoted as *porous airfoil*) are compared with those obtained for a solid baseline configuration (*solid airfoil*) and for a wing profile entirely made of melamine foam (*melamine airfoil*). Far-field aeroacoustic measurements highlight a noise reduction up to 2 dB at low frequencies that is more pronounced in correspondence with the vortex-shedding frequency peak and a noise increase at high frequencies. The presence of the exoskeleton does not significantly affect the former effect but has a striking impact on the second one, enhancing the sound generation due to the interaction between the flow and the pores of the hard-plastic component.
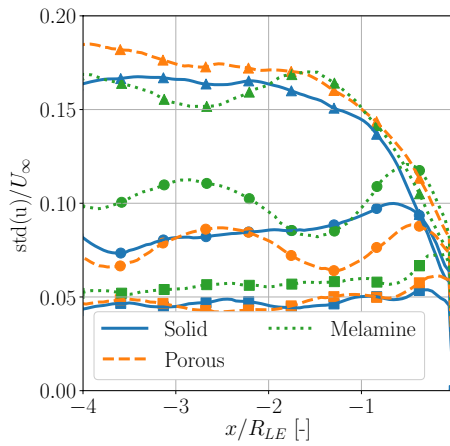
(a) Streamwise turbulence intensity
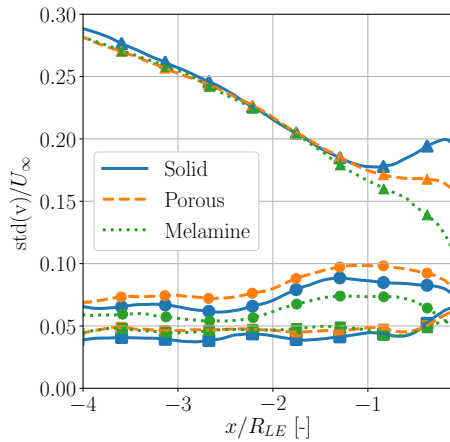
(b) Upwash turbulence intensity
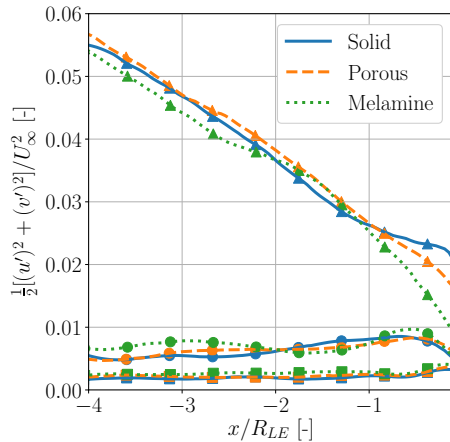
(c) TKE

Fig. 16 Turbulence quantities extracted along the stagnation streamline for different airfoil configurations (solid ——, porous ▪▪▪▪, melamine ▪▪▪▪) and different POD decompositions (0 − 50% △; 50 − 70% ○; 70 − 90% □)
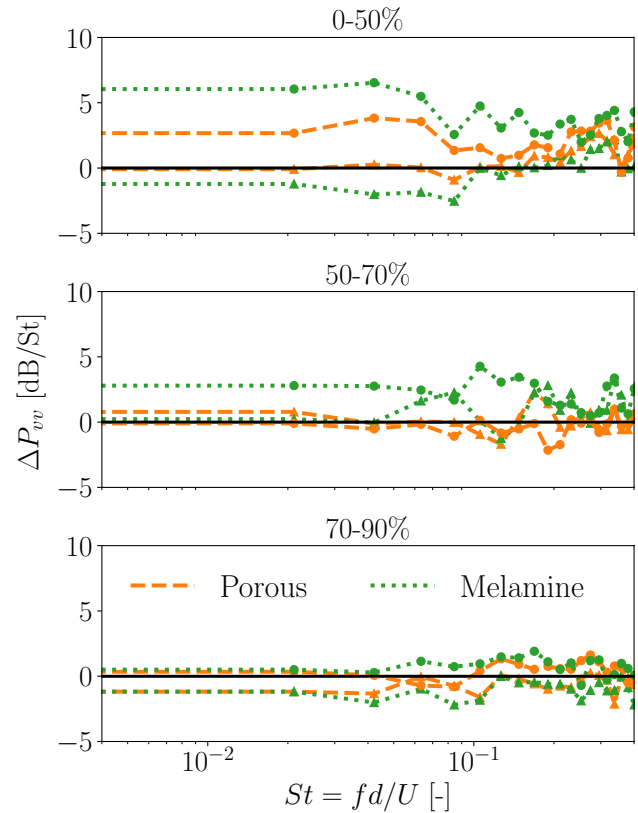

Fig. 17 Relative local spectra of the upwash velocity component with reference to the solid case, obtained with POD reconstructions of the flow at $(x, y)/R_{LE} = (-0.25, 0)$. △: inflow $(x, y)/R_{LE} = (-3, 0)$; ○: stagnation region $(x, y)/R_{LE} = (-0.25, 0)$

The PIV results indicate that the porosity alters the flow field in different ways. Firstly, it influences the flow acceleration in the region of higher curvature of the airfoil. Secondly, it affects the turbulence intensity variation along the stagnation streamline from the upstream values. In particular, both decrease in the streamwise turbulent velocity component and increase in the upwash turbulent velocity component are mitigated by the porous treatments of the airfoils. The presence of an exoskeleton, which is essential to preserve the profile shape and the aerodynamic performance of the airfoil, partially impairs this mitigation effect. The extent of the region at which porosity has an impact on the velocity field and the magnitude of the deviation are found to be directly proportional to the Reynolds number.

Subsequently, the POD is used to filter out the different turbulence scales of the flow, following a decomposition approach based on energy bins that are defined according to the eigenvalues of the energy matrix. The comparison of the reconstructed flows for solid and porous airfoil configurations is made possible by the relatively good agreement of the inflow turbulence conditions, which have been studied

by means of a spatial Fourier analysis. The results show that the alterations in the flow field due to porosity mostly involve the low-frequency range of the velocity spectrum, reconstructed with the most energetic modes of the POD algorithm, in accordance with the aeroacoustic results. The present work thereby provides a better understanding of the attenuation of the distortion experienced by turbulence in the interaction with a porous airfoil, which can, in turn, give an insight into the physical mechanisms involved in the corresponding noise reduction.

Declarations

Conflict of interest The authors declare that they have no conflict of interest.

References

Amiet R (1975) Acoustic radiation from an airfoil in a turbulent stream. J Sound Vib 41(4):407–420. https://doi.org/10.1016/S0022-460X(75)80105-2

Amiet R (1976) Noise due to turbulent flow past a trailing edge. J Sound Vib 47(3):387–393. https://doi.org/10.1016/0022-460X(76)90948-2

Bampanis G, Roger M (2020) On the turbulence-impingement noise of a naca-12 airfoil with porous inclusions. In: AIAA AVIATION 2020 FORUM, AIAA. https://doi.org/10.2514/6.2020-2577

Bingham H, Larsen P, Barker V (2018) Computational Fluid Dynamics. Technical University of Denmark, DK-2800 Kongens Lyngby, Denmark

Brindise M, Vlachos P (2017) Proper orthogonal decomposition truncation method for data denoising and order reduction. Exp Fluids 58. https://doi.org/10.1007/s00348-017-2320-3

Cenedese A, Miozzi M, Querzoli G (1997) Comparison between fourier and proper orthogonal decomposition of a velocity field within a convective vessel. In: Proceedings of the 8th international conference on computational methods and experimental measurements, computational mechanics publications, 1:319–329

Deri E, Braza M, Cid E, Cazin S, Michaelis D, Degouet C (2014) Investigation of the three-dimensional turbulent near-wake structure past a flat plate by tomographic piv at high reynolds number. J Fluids Struct 47:21–30. https://doi.org/10.1016/j.jfluidstructs.2012.11.005

Devenport WJ, Staubs JK, Glegg SAL (2010) Sound radiation from real airfoils in turbulence. J Sound Vib 329(17):3470–3483. https://doi.org/10.1016/j.jsv.2010.02.022

Foucaut JM, Carlier J, Stanislas M (2004) PIV optimization for the study of turbulent flow using spectral analysis. Meas Sci Technol 15(6):1046–1058. https://doi.org/10.1088/0957-0233/15/6/003

Garcia D (2010) Robust smoothing of gridded data in one and higher dimensions with missing values. Comput Stat Data Anal 54(4):1167–1178. https://doi.org/10.1016/j.csda.2009.09.020

Geyer T, Sarradj E, Fritzsche C (2010) Measurement of the noise generation at the trailing edge of porous airfoils. Exp Fluids 48(2):291–308. https://doi.org/10.1007/s00348-009-0739-x

Geyer T, Sarradj E, Giesler J, Hobracht M (2011) Experimental assessment of the noise generated at the leading edge of porous airfoils using microphone array techniques. In: 17th AIAA/CEAS aeroacoustics conference 2011 (32nd AIAA Aeroacoustics Conference). https://doi.org/10.2514/6.2011-2713

Geyer T, Sarradj E, Giesler J (2012) Application of a beamforming technique to the measurement of airfoil leading edge noise. Advances in Acoustics and Vibration 2012: https://doi.org/10.1155/2012/905461

Graftieaux L, Michard M, Grosjean N (2001) Combining piv, pod and vortex identification algorithms for the study of unsteady turbulent swirling flows. Meas Sci Technol 12:1422. https://doi.org/10.1088/0957-0233/12/9/307

Howe MS (1991) Surface pressures and sound produced by turbulent flow over smooth and rough walls. J Acoust Soc Am 90(2):1041–1047

Jacob M, Boudet J, Casalino D, Michard M (2005) A rod-airfoil experiment as a benchmark for broadband noise modeling. Theor Comput Fluid Dyn 19:171–196. https://doi.org/10.1007/s00162-004-0108-6

Kroeger RA, Grushka HD, Helvey TC (1972) Low speed aerodynamics for ultra-quiet flight. Tech. Rep. AD893426, Air force flight dynamics laboratory Wright-Patterson Air Force Base, Ohio

Liu Y, Dowling A, Shin HC (2006) Effects of surface roughness on airframe noise. In: 12th AIAA/CEAS Aeroacoustics Conference (27th AIAA Aeroacoustics Conference), American Institute of Aeronautics and Astronautics, Cambridge, MA

Liu Y, Dowling A, Shin HC, Quayle A (2007) Experimental study of surface roughness noise. In: 13th AIAA/CEAS Aeroacoustics Conference (28th AIAA Aeroacoustics Conference), American Institute of Aeronautics and Astronautics, Rome, Italy

Lumley JL (1967) The structure of inhomogeneous turbulence. In: Atmospheric turbulence and wave propagation, Nauka, Moscow, Russia

Melling A (1997) Tracer particles and seeding for particle image velocimetry. Meas Sci Technol 8(12):1406–1416. https://doi.org/10.1088/0957-0233/8/12/005

Mendez MA, Hess D, Watz BB, Buchlin JM (2020) Multiscale proper orthogonal decomposition (mpod) of tr-piv data-a case study on stationary and transient cylinder wake flows. Meas Sci Technol 31(9): https://doi.org/10.1088/1361-6501/ab82be

Merino-Martinez R, Rubio Carpio A, Pereira L, Herk S, Avallone F, Ragni D, Kotsonis M (2020) Aeroacoustic design and characterization of the 3d-printed, open-jet, anechoic wind tunnel of delft university of technology. Appl Acoust 170: https://doi.org/10.1016/j.apacoust.2020.107504

Migliore P, Oerlemans S (2004) Wind tunnel aeroacoustic tests of six airfoils for use on small wind turbines. J Sol Energy Eng 126(4):974–985

Moreau S, Roger M (2005) Effect of angle of attack and airfoil shape on turbulence-interaction noise. In: Collection of technical papers - 11th AIAA/CEAS aeroacoustics conference, vol 3. https://doi.org/10.2514/6.2005-2973

Ninni D, Mendez MA (2020) Modulo: a software for multiscale proper orthogonal decomposition of data. 2004.12123

Niskanen M, Groby JP, Duclos A, Dazel O, Le Roux JC, Poulain N, Huttunen T, Lähivaara T (2017) Deterministic and statistical characterization of rigid frame porous materials from impedance tube measurements. J Acoust Soc Am 142(4):2407–2418. https://doi.org/10.1121/1.5008742

Olsen W, Wagner J (1982) Effect of thickness on airfoil surface noise. AIAA J 20(3):437–439. https://doi.org/10.2514/3.7922

Paruchuri C, Joseph P, Chong T, Priddin M, Ayton L (2020) On the noise reduction mechanisms of porous aerofoil leading edges. J Sound Vib 485: https://doi.org/10.1016/j.jsv.2020.115574

Paterson R, Amiet R (1976) Acoustic radiation and surface pressure characteristics of an airfoil due to incident turbulence. In: 3rd AIAA/CEAS aeroacoustic conference. https://doi.org/10.2514/6.1976-571

Pope SB (2000) Turbulent Flows. Cambridge University Press. https://doi.org/10.1017/CBO9780511840531

Raiola M, Discetti S, Ianiro A (2015) On PIV random error minimization with optimal POD-based low-order reconstruction. Exp Fluids 56(56):75. https://doi.org/10.1007/s00348-015-1940-8

Roger M, Moreau S (2016) Airfoil turbulence-impingement noise reduction by porosity or wavy leading-edge cut: experimental investigations. In: 45th International Congress and Exposition on Noise Control Engineering, INTER-NOISE, Hamburg, Germany

Roger M, Schram C, Santana LD (2013) Reduction of airfoil turbulence-impingement noise by means of leading-edge serrations and/or porous material. In: 19th AIAA/CEAS aeroacoustics conference. https://doi.org/10.2514/6.2013-2108

Sarradj E, Geyer T (2007) Noise generation by porous airfoils. In: 13th AIAA/CEAS aeroacoustics conference (28th AIAA Aeroacoustics Conference), AIAA paper. https://doi.org/10.2514/6.2007-3719

Satcunanathan S, Meinke M, Schröder W (2019) Prediction of noise mitigation by porous media based on a direct-hybrid cfd/caa method. In: 25th AIAA/CEAS aeroacoustics conference. https://doi.org/10.2514/6.2019-2696

Satcunathan S, Zamponi R, Meinke M, Van de Wyer N, Schram C, Schröder W (2019) Validation of a model for acoustic absorption in porous media. In: 48th International congress and exhibition on noise control engineering, INTER-NOISE, Madrid

Scarano F, Moore P (2011) An advection-based model to increase the temporal resolution of piv time series. Exp Fluids 52:919–933. https://doi.org/10.1007/s00348-011-1158-3

Schrijer FFJ, Scarano F (2008) Effect of predictor-corrector filtering on the stability and spatial resolution of iterative PIV interrogation. Exp Fluids 45(5):927–941. https://doi.org/10.1007/s00348-008-0511-7

Sciacchitano A, Wieneke B (2016) PIV uncertainty propagation. Meas Sci Technol 27(8): https://doi.org/10.1088/0957-0233/27/8/084006

Tandalam A, Balachandar R, Barron R (2010) Reynolds number effects on the near-exit region of turbulent jets. J Hydraul Eng 136(9):633–641. https://doi.org/10.1061/(ASCE)HY.1943-7900.0000232

Teruna C, Avallone F, Casalino D, Ragni D (2020) Numerical investigation of leading edge noise reduction on a rod-airfoil configuration using porous materials and serrations. J Sound Vib 494: https://doi.org/10.1016/j.jsv.2020.115880

Towne A, Schmidt OT, Colonius T (2018) Spectral proper orthogonal decomposition and its relationship to dynamic mode decomposition and resolvent analysis. J Fluid Mech 847:821–867. https://doi.org/10.1017/jfm.2018.283

Welch P (1967) The use of fast fourier transform for the estimation of power spectra: a method based on time averaging over short, modified periodograms. IEEE Trans Audio Electroacoust 15(2):70–73. https://doi.org/10.1109/TAU.1967.1161901

Westerweel J (1997) Fundamentals of digital particle image velocimetry. Meas Sci Technol 8(12):1379–1392. https://doi.org/10.1088/0957-0233/8/12/002

Westerweel J, Dabiri D, Gharib M (1997) The effect of a discrete window offset on the accuracy of cross-correlation analysis of digital PIV recordings. Exp Fluids 23(1):20–28. https://doi.org/10.1007/s003480050082

Wieneke B (2015) PIV uncertainty quantification from correlation statistics. Measur Sci Technol 26. https://doi.org/10.1088/0957-0233/26/7/074002

Zamponi R, Ragni D, Van de Wyer N, Schram C (2019) Experimental investigation of airfoil turbulence-impingement noise reduction using porous treatment. In: 25th AIAA/CEAS aeroacoustics conference, 2019, AIAA. https://doi.org/10.2514/6.2019-2649

Zamponi R, Satcunanathan S, Moreau S, Ragni D, Meinke M, Schröder W, Schram C (2020) On the role of turbulence distortion on leading-edge noise reduction by means of porosity. J Sound Vib 485: https://doi.org/10.1016/j.jsv.2020.115561

Zamponi R, Moreau S, Schram C (2021) Rapid distortion theory of turbulent flow around a porous cylinder. J Fluid Mech 915:A27. https://doi.org/10.1017/jfm.2021.8

Publisher's Note Springer Nature remains neutral with regard to jurisdictional claims in published maps and institutional affiliations.